Research Article Vol. 3, No. 1 / 15 Jan 2024 / Optics Continuum 9
OPTICS CONTINUUM

Krypton tagging velocimetry in the plume of a plasma hollow cathode

JACOB A. GOTTFRIED AND AZER P. YALIN*

Department of Mechanical Engineering, Colorado State University, Fort Collins, CO 80521, USA
*Azer.Yalin@colostate.edu

Abstract: Krypton tagging velocimetry (KTV) is an emerging flow diagnostic that investigates the bulk movement of high-speed, low-pressure gas flows. The present contribution expands the typical KTV method to the lower density (vacuum) conditions of interest in electric propulsion research. Our KTV scheme utilizes a two-photon (Write) excitation at 214.7 nm from a pulsed dye laser, followed by (Read) re-excitation of the ensuing metastable at 769.5 nm with an optical parametric oscillator. For the case of cold krypton gas expanding from a hollow cathode into vacuum, we find a bulk velocity of 452 ± 37 m/s and temperature of 20 ± 16 K. We also study the flow in the plume with the hollow cathode plasma operating for which we find bulk velocity of 1200 ± 130 m/s and temperature of 880 ± 370 K. Measurements are performed at background pressures down to $\sim 10^{-5}$ Torr.

1. Introduction

Since electric propulsion for spacecraft was first proposed in the early 1900s, electric propulsion thrusters such as Hall-effect thrusters and ion thrusters have found place in a variety of applications ranging from deep space exploratory missions to satellite station keeping. A vital subassembly of these thrusters is the plasma hollow cathode which acts as both a plume neutralizer and electron source in the case of Hall-effect thrusters [1]. In addition to plasma propulsion, plasma hollow cathodes find use in applications including surface processing [2–4] and as ionization sources for neutral beam injection within fusion devices [5–7]. Due to the importance of these devices, significant work has gone into developing computational models of their operation, both to inform the development of future designs as well as to elucidate the complex phenomenon observed in their operation [8–13].

Experimental measurements, in particular looking at spatially resolved flow-fields (density, temperature, velocity), are critical to elucidate the physics of the devices and for model validation [14–21]. With regards to characterizing velocity fields, laser induced fluorescence (LIF) velocimetry, based on Doppler shifting of an absorbing metastable level, is commonly used to measure velocity distribution functions (VDFs) of both neutrals and ions [15–18,22,23]. In general, LIF velocimetry produces accurate VDF values but it is complicated, and its resolution is limited, by the hyperfine structure of the absorbing transition [24]. Commonly used LIF velocimetry probes a metastable (containing a low fraction of the overall population, i.e., $<\sim$0.1-1%) which can potentially introduce bias to the recorded VDF, for example owing to varying degrees of exciting the metastable due to varying electron temperature in time-resolved measurements [23–25]. The fact that the LIF probes a metastable is also limiting in terms of being able to infer (overall) density since the population fraction of the probed level can vary in complex ways [23]. Owing to this concern, measurements of the neutral number density are commonly performed using two-photon absorption LIF (TALIF) to directly probe the ground state (containing a large fraction of the overall population) [17,26–30].

Herein, we investigate krypton tagging velocimetry (KTV) as an alternative diagnostic to measure neutral velocity distributions within electric propulsion (EP) devices. KTV is a form of velocimetry which directly interrogates the bulk movement of atoms by tagging ground state

#503138 https://doi.org/10.1364/OPTCON.503138
Journal © 2024 Received 17 Aug 2023; accepted 12 Dec 2023; published 18 Dec 2023

OPTICS CONTINUUM

atoms through TALIF (where fluorescence populates a metastable state), and then reading the location of tagged atoms at a later point in time through a second (single-photon) LIF step. As such, it is part of a larger class of two-step Read-Write flow-tagging diagnostics which also includes the RELIEF technique (which uses Raman excitation and LIF to Write and Read oxygen molecules [31]) as well as other two-step LIF techniques based on reading long-lived (tagged) metastable states [32,33]. Therefore, KTV allows for the ground state density to be directly measured (by monitoring the TALIF signal) *and* for the velocity of ground state atoms to be directly measured based on their spatial displacement (between the Write and Read steps). To date, KTV has been successfully applied to a variety of flows using krypton as a seed gas including sonic and supersonic over-expanded jets [34,35], Mach 3 turbulent boundary layers [36], and in hypersonic shock tube flows at repetition rates up to 100 kHz [37–39]. The use of Kr is attractive in these applications because it is an inert additive (generally to air or N_2), whereas in EP it is suitable due to its growing use as a propellant.

In this contribution we show the use of KTV to record Kr velocity profiles at low pressure conditions in hollow cathodes, both for cold-flow and operating plasma conditions. Section 2 of this paper details the spectroscopic scheme used in this work, followed by Section 3 describing the optical and experimental setup used to employ the KTV scheme. Section 4 provides our data analysis methodology for a fiber optic-based collection system, followed by Section 5 providing the results for both a cold gas expansion into a vacuum as well as within a plasma plume generated by a hollow cathode. Finally, Section 6 will provide our conclusions and future work on this topic.

2. Krypton tagging velocimetry spectroscopic scheme

Previous publications have detailed a variety of spectroscopic schemes for KTV including two-laser schemes utilizing TALIF excitation at 216 or 214 nm [34,36,37,40,41] and simplified single-laser schemes using 212 nm excitation [35,42,43]. For an EP application, we consider the Kr flow-field in the plume of a hollow cathode. The plasma environment complicates KTV as there can be significant natural population (providing optical interference) in the same metastable state that is probed in the Read step. (Collisional-radiative models show expected level populations of the metastables of <~1% of the total population.) Expected velocities are ~300-1,500 km/s which calls for Read-Write time delays of order microseconds to achieve resolvable movement with our collection system. Due to these constraints, a scheme using 214.7 nm TALIF excitation is considered optimal. Further, previous works from our group investigating neutral krypton densities within a hollow cathode plasma have shown strong TALIF signal-to-noise with this scheme [26,30]. Figure 1 shows the relevant transitions associated with a 214.7 nm Write step where Table 1 provides the transition details.

Table 1. Relevant krypton transitions

TRANSITION	$\lambda_{Air}[nm]$	# PHOTONS	$A_{ik}\ [s^{-1}]$	$E_i\ [cm^{-1}]$	$E_k\ [cm^{-1}]$	LOWER LEVEL	UPPER LEVEL
A	214.7	Two-Photon	-	0	93123.34	$4s^24p^6(^1S_0)$	$5p[3/2]_2$
B	760.2	Single-Photon	2.732×10^7	79971.74	93123.34	$5s[3/2]^\circ_2$	$5p[3/2]_2$
C	769.454	Single-Photon	4.27×10^6	79971.74	92964.39	$5s[3/2]^\circ_2$	$5p[3/2]_1$
D	829.811	Single-Photon	2.93×10^7	80916.76	92964.39	$5s[3/2]^\circ_1$	$5p[3/2]_1$

The Write step (also referred to as tagging) is performed with two-photon excitation using 214.7 nm ($4s^24p^6(^1S_0) \rightarrow 5p[3/2]_2$); transition A in Fig. 1. From the upper level excited state, the atom will decay to the lower lying metastable state $5p[3/2]_2 \rightarrow 5s[3/2]^\circ_2$ releasing a photon at 760.2 nm, transition B, with 0.76 branching ratio [40]. *The Read step* is performed with a single photon excitation at 769.5 nm ($5s[3/2]^\circ_2 \rightarrow 5p[3/2]_1$, transition C). The fluorescence (KTV)

OPTICS CONTINUUM

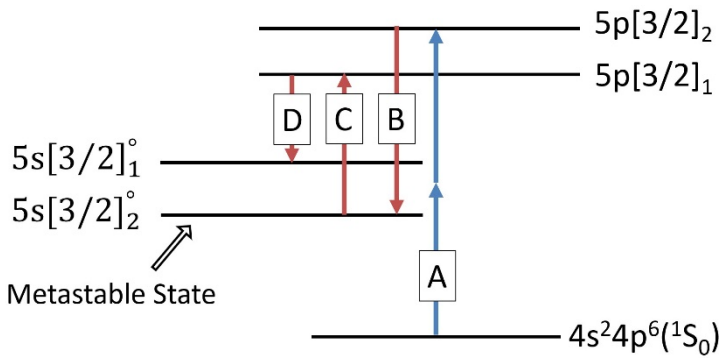

Fig. 1. KTV Energy level diagram with relevant transitions. "A - Write laser (214.7 nm)", "C - Read laser (769.4 nm)", and "D - Read signal (829.8 nm)".

signal collected from the Read step is at 829.8 nm ($5p[3/2]_1 \rightarrow 5s[3/2]^\circ_1$, transition D) as this transition is optically separated from all laser wavelength and has a favorable branching ratio of ~0.85 [44,45].

3. Optical layout and experimental setup

The Write step is performed with a dye laser (Sirah PrecisionScan) pumped by the third harmonic output of a Nd:YAG laser (Spectra-Physics Quanta Ray Lab 150-10). The dye laser uses Exalite 428 dye and produces visible light at ~429 nm which is then frequency-doubled to ~214.7 nm using an internal frequency conversion unit. The final laser output is an approximately rectangular beam ~2 mm by ~6 mm in size with pulse energy of ~2.5 mJ. The beam is delivered such that the longer dimension is into the page as depicted in Fig. 2. The beam is brought to a weak focus with a 75 cm plano-convex lens with the focal spot on the hollow cathode centerline at a position ~0.75 cm downstream of the keeper orifice plate. The resulting fluence is ~2 J/cm^2, a value lower than typically used for KTV [34] due to spatial restrictions of the chamber (for robust operation, the write laser focusing lens is located outside of the vacuum chamber which limits the minimum beam waist) and maximum dye laser output.

The Read laser is an optical parametric oscillator (OPO, Continuum Sunlite III) pumped by the third harmonic output of a Nd:YAG (Continuum Powerlite 8010). The resulting output is at 769.5 nm with an average pulse energy of ~2 ± 1 mJ. This energy is far above the saturation threshold of the strong single-photon LIF transition [37] and a neutral density filter (optical density of 6) is used to lower the output energy. A spatial filter, based on a focused beam through a pinhole, serves to improve the beam quality of the OPO output Read beam. The filter uses a plano-convex lens pair (7.5 cm and 15 cm focal lengths) between which a 100 µm pinhole is positioned. To further improve the signal-to-noise (S:N), the Read laser is converted to a sheet of approximately 1 cm in height and ~300 µm thick within the measurement region by a spherical plano-convex (1 m focal length) and cylindrical plano-convex lens (50 cm focal length). The energy and spatial filtering of the Read beam are essential to achieving high S:N, by controlling the volume over which the Read laser probes (to minimize the amount of background fluorescence generated outside of the volume containing the tagged atoms), given the aforementioned challenge of strong fluorescence associated with LIF of naturally occurring metastables (that can quickly overwhelm the KTV portion added by the Write step). However, the spatial filter would become less significant if a diode laser is used for the read step rather than an OPO (see also discussion in the Conlcusion). For both lasers, the wavelength is tuned such that the maximum Read fluorescence signal is obtained. The OPO wavelength is monitored with a wavelength meter

OPTICS CONTINUUM

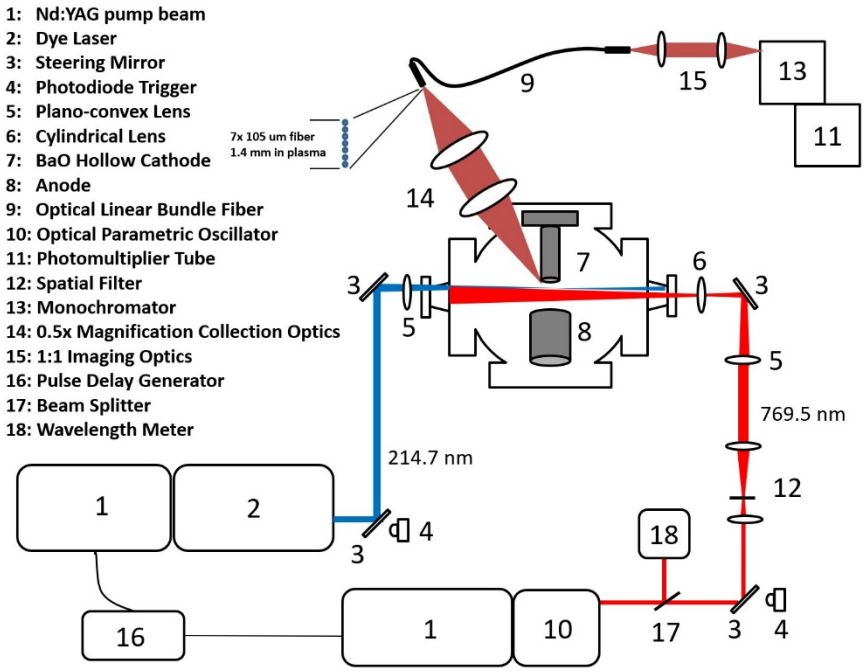

Fig. 2. Optical layout for krypton tagging velocimetry.

(HighFinesse WS4) and the dye laser wavelength output is monitored by periodically checking the peak of the TALIF signal.

The fluorescence signal is collected orthogonally to the plane of the Read laser sheet (and cathode centerline axis) through a vacuum chamber window with a 30 cm focal length, 5 cm diameter plano-convex lens. The collected LIF Read signal, including plasma luminous emission from the region, is imaged onto a linear 7×105 µm multi-mode optical fiber bundle (Thorlabs BFA105LS02) with a 15 cm focal length, 5 cm diameter plano-convex lens resulting in a magnification of 0.5 and an approximate collection area (in the cathode plume) of 1.4 mm by 210 µm. The longer dimension of the imaging volume is parallel to the Read laser (perpendicular to the cathode axis). The collection optics are implemented within an optical cage assembly which is located on a linear translation stage (allowing one to change the sampling location along the cathode axis direction and relative to the Write laser). The output of the optical fiber bundle is one-to-one imaged onto a monochromator (0.25 m focal length, EG&G Model 1229) with a 1 mm entrance slit. The monochromator is not scanned but is used as a wavelength filter to preferentially collect light at the detection wavelength of 830 nm while rejecting light from nearby Kr and Kr + emission lines. The orientation of the fiber output is set with the longer dimension parallel to the slit. The collected light is dispersed with a 1200 g/mm grating blazed at 750 nm (Edmund Optics 43211) onto the output slit set to 1 mm. The resulting spectral range exiting the output slit is approximately 830 ± 6 nm. The output light of the monochromator is detected with a photomultiplier tube (Hamamatsu R3896) with the gain set to 900 V (corresponding to a gain of 3×10^6 based on the manufacturer's datasheet).

The timing of the two lasers is controlled by a pulse delay generator (Stanford Research Instruments DG-535). Although the delay generator maintains sub-picosecond jitter, the relative jitter between output of the two lasers is described roughly as a histogram of Gaussian form with a full-width half-max (FWHM) of approximately 65 ns. The timing of the photomultiplier tube

OPTICS CONTINUUM

collection is controlled by an oscilloscope triggering off the Read laser photodiode positioned (Fig. 2).

The data collection procedure consists of positioning the optical fiber bundle at a known downstream displacement from the Write laser. For each position, the time delay between the Write and Read lasers is swept over an appropriate range in 0.1 μs increments. At each time step, the Read LIF signal (830 nm light to PMT) is collected and averaged for 100 laser pulses. In the case of plasma measurements, the process is completed twice due to lower signal-to-noise. The result of this method is the temporal evolution of the LIF signal for the given spatial displacement (between Write-Read locations), i.e., each recorded signal corresponds to the number of starting Kr atoms (from the Write region) having the velocity needed to traverse the given displacement in the given time delay. As such, the recorded data contains information about the velocity distribution, for example the time-delay yielding the largest signal would correspond to the most probable velocity of the distribution. Below, we discuss inclusion of more detailed analysis issues associated with spatial broadening of the beams and light collection, and temporal jitter of the lasers.

This work investigates both the cold gas flow and plasma generated by a 25 A class barium oxide (BaO) heater-less hollow cathode developed at Colorado State University and Plasma Controls LLC which is operated under high vacuum conditions (1×10^{-6} Torr base pressure, 4×10^{-4} Torr during operation). The cathode is centrally mounted within an approximately spherical vacuum chamber (diameter ~0.6 m) equipped with a turbomolecular pump (Agilent TV1001) backed by a roughing pump. The hollow cathode is operated in a propellent rich spot-mode produced by 15 SCCM mass flow rate of krypton gas (99.999%) and an anode current of 5 A (along with a keeper current of 1 A). The mass flow rate is controlled by a digital mass flow controller (Unit Instruments 7360). The anode and keeper are driven under constant current operation where the associated voltages are nominally 45 and 7 V respectively during steady state operation. Figure 3 is an image of the hollow cathode plasma where the red box represents the area over which the KTV is performed (roughly to scale). The actual light collection region for a given measurement, defined by the image of the fiber bundle in this plane, would be a narrower horizontal stripe within this rectangle.

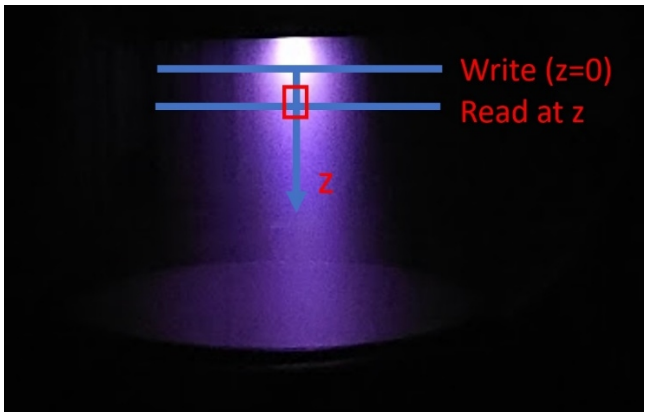

Fig. 3. Image of the plasma hollow cathode operating with an overlay of Write and Read geometry (approx. to scale).

4. Data analysis

For a given spatial displacement (between Read and Write beams) and cathode measurement condition, the Read fluorescence is measured at a series of delay times (again Read relative to

OPTICS CONTINUUM

Write) to map out the arrivals of the tagged atoms to the Read region. Raw LIF signals from the PMT are processed with a custom LabVIEW code (developed for TALIF neutral density measurements [26]) which subtracts background and temporally-integrates the LIF signals. In the simplest analysis, the temporal profile of LIF signal versus delay time can be converted to a velocity distribution by associating a velocity with each delay time as v = L/t (where L is the displacement length and t is the delay time). However, such an approach neglects various systematic effects of spatial and temporal blurring which otherwise provide some biases (e.g., artificial broadening of the resulting velocity profile due to the finite spatial extents of both the Write and Read regions).

To determine the actual drift velocity and VDF, the true temporal signal should be deconvolved from the broadening effects of the spatial distributions (due to the Write beam and the collection fiber). However, a direct deconvolution is computationally expensive and therefore we adopt an iterative gradient decent method based on fitting simulated temporal signals to the measured data and seeking the best agreement based on a squared error loss function. The possible temporal signals are calculated as the convolution of the velocity profile, f, with the spatial response w:

$$S(t) = \int_{-\infty}^{\infty} w(z') \cdot f\left(\frac{z+z'}{t}\right) dz' \tag{1}$$

where z is the nominal Read (fiber) displacement relative to the Write beam, z' is the integrating variable corresponding to the position with respect to the center of the Read collection volume, t is time, $w(z')$ is a spatial weighting function (centered at zero) associated with both the TALIF Write step and the Read step (imaging extent of the fibers), and $f(V_z)$ is the assumed velocity distribution function. The velocity distribution functions assume a single-component Maxwell-Boltzmann distribution, specified by a temperature, along with a bulk velocity, with peak amplitude normalized to unity:

$$f(V_z) = e^{\frac{-m_{Kr}(V_z - V_d)^2}{2kT}} \tag{2}$$

where k is the Boltzmann constant, m_{Kr} is the atomic mass of krypton, T is the bulk gas temperature (defining the velocity broadening), and V_d is the bulk drift velocity. The single-component form is used as we anticipate primarily 1-D flows along the cathode center line direction and because our measurement is sensitive to the single flow direction.

To determine the overall spatial response function of the experiment, including effects of both the Write laser and the fiber optic (Read) collection, the spatial distribution of the Write laser TALIF signal is measured by scanning the optical fiber across the laser's waist position. (We find that the resulting spatial weighting function is approximately Lorentzian with a half-width at half-maximum of ~0.2 mm.) The result of the spatial measurement is used to empirically set the weighting function used in the convolution process according to the normalization condition:

$$\int_{-\infty}^{\infty} w(z')\, dz' = 1 \tag{3}$$

Using Eqs. (1)–(3), a simulated $S(t)$ is fit to a set of experimental temporal signals (at different delays) using a minimization of the difference of squares, finding the best V_d and T to describe the data. This fitting process is also performed at several fiber displacements (based on the corresponding temporal LIF signals), providing inference of the Kr atom velocity and temperature as measured at each displacement. Figure 4 is an example of the fitting performed on raw data for a cold gas flow expansion into a vacuum (where we normalize the peak temporal signal for each displacement to unity).

An important detail regarding our setup is that, for small spatial displacements (<~0.7 mm), there is an overlap between the wings of the initial Write step spatial distribution (~0.6 mm in

OPTICS CONTINUUM

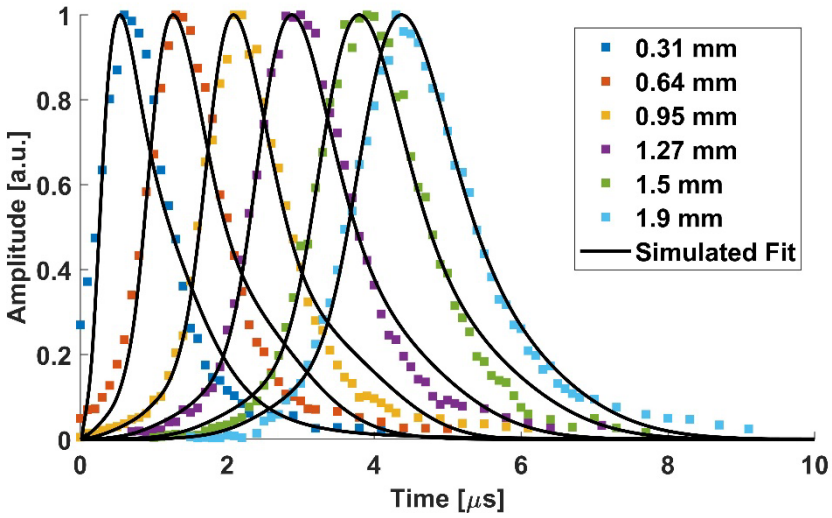

Fig. 4. Overlay of simulated fit and the normalized experimental data for cold krypton expansion into a vacuum.

axial extent) with the fiber imaging volume (~0.1 mm in axial extent). This overlap fundamentally precludes measurements for these small displacements (since measured particles cannot be unambiguously associated with known displacement distances) and biases the fit to artificially high velocities. When the overlap is combined with further sources of error such as laser timing jitter and a 0.1 mm uncertainty in absolute fiber displacement (z in Eq. (1)), it is found that the fiber displacements of 0.31 and 0.64 mm do not have sufficient displacement (from the Write location) to accurately perform the deconvolution process. (These results are shown in Fig. 4 only for purposes of exposition and are not used in subsequent analyses.)

The error in the fitting and deconvolution process is handled in two parts, considering the spatial and temporal uncertainties, by recomputing the fitting process at the extrema of the uncertainty ranges applied to the fiber displacement and time axis. The numerical fit error is then calculated through:

$$Error_N = \sqrt{diag(H^{-1})} \tag{4}$$

where H is the Hessian matrix numerically approximated by the finite difference method on the divergence of the error in the difference of squares between the experimental data and the fit. The overall error reported in the results is finally found as the root sum squared of the independent error sources (i.e., error contributions due to the timing jitter between the Write and Read lasers, the uncertainty in the absolute fiber displacement values, and the error within the fitting algorithm).

5. Results and discussion

The first results presented are the cold gas expansion through the hollow cathode and its output orifice into the vacuum chamber (data shown in Fig. 4). A cold gas expansion is used for verification of the data analysis method as it presents a high signal-to-noise measurement environment in a condition where the physics are relatively well understood. Figure 5 shows the best-fit drift velocities and temperatures associated with the fits and profiles from Fig. 4.

The cold gas expansion results shown in Fig. 5 appear quite constant for different spatial displacements (downstream Read positions) yielding an average velocity of 452 ± 37 m/s and average temperature of 20 ± 16 K. Although one would typically expect to see the evolution of

OPTICS CONTINUUM

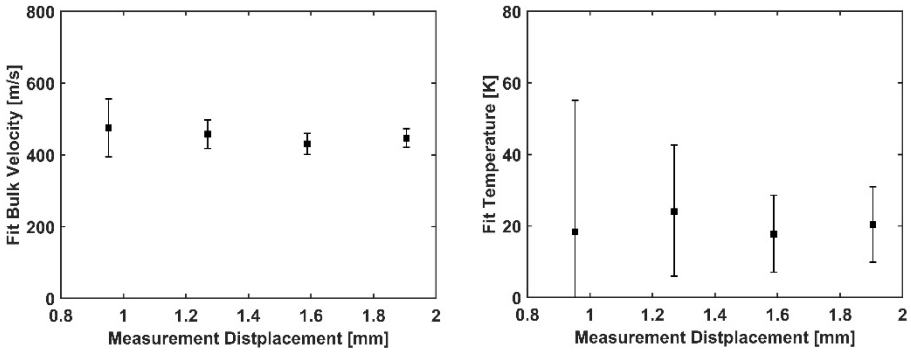

Fig. 5. Average bulk velocity and temperature for cold krypton expansion into a vacuum.

gas properties over space, it is important to realize the present measurements are taken in a nearly collisionless regime where the Knudsen number is order unity or larger (mean free paths on the order of several to tens of centimeters [30,46]). Therefore, over the displacements used in this work (<~2 mm), it is unlikely for a tagged atom to experience even a single collision such that the flow properties are essentially frozen at the conditions present at the location of the Write beam. Conversely, if one were to apply KTV with fiber displacements on the order of or greater than the mean free path, varying properties would be observed.

As a rough check on measurement accuracy, the expected temperature and velocity are calculated using adiabatic expansion equations from Engeln et. al. for a plasma expanding into a vacuum [47]. The temperature is calculated by:

$$\frac{T(z)}{T_0} = \left(\frac{n(z)}{n_0}\right)^{\gamma-1} \tag{5}$$

where T is the temperature, n is the neutral density, and γ is the ratio of specific heats for krypton. Approximate values for the neutral density both within the cathode and at the measurement location are determined from past TALIF work and simulation results [30]. From Eq. (5), we find that the predicted temperature at the measurement location is in the range of 20–30 K. The maximum velocity due to adiabatic expansion, assuming a sonic point at the cathode orifice, is calculated from:

$$V_{max} = c_{s_0}\sqrt{\frac{\gamma+1}{\gamma-1}} \tag{6}$$

where c_{s_0} is the speed of sound at the cathode orifice [47]. Assuming pure krypton and T_0 of 300 K, the maximum velocity is approximately 445 m/s. For both the temperature and bulk velocity, the adiabatic expansion calculations result in values that are within the error range of the experimental measurements. Furthermore, numerical simulations of argon expansion through nozzles in the near continuum flow regime resulted in similar bulk velocities and temperatures [48]. Based on these findings, the temperature and velocity values are considered reasonable within their respective error ranges.

To the best of the authors' knowledge, these results represent the first direct measurement of ground state neutral atom properties undergoing vacuum expansion, as well as being the KTV data reported at the lowest pressures to date (first useful at EP conditions). We have demonstrated KTV at background chamber pressures as low as 10^{-5} Torr (results shown in Fig. 4 correspond to 4×10^{-4} Torr), which is 2–3 orders of magnitude below the lowest pressures at which KTV has been previously applied (2.5 Torr with 1% Kr [34]). With regards to Read signal loss owing to quenching of the metastable, we find a characteristic quench time of >1 ms at pressure of

OPTICS CONTINUUM

10^{-4} Torr, such that signal loss by this mechanism seems negligible at the conditions of present interest. (The quench time can be simply estimated as $1/(k_Q N_{Kr})$, where k_Q is the Kr self-quench rate for which we use 1.7×10^{-10} cm^3 s^{-1} based on the rate for another Kr excited state [49] and N_{Kr} is the number density of Kr colliders for which we use $N_{Kr} \sim 4 \times 10^{12}$ cm^{-3}.)

Following the validation of cold gas expansion, the next condition investigated is within the plasma plume of the hollow cathode operating on krypton. Within a plasma environment, there are added complications including a lower neutral density (due to both ionization and expansion from an increased temperature) and an increase in the (background) population fraction within the $5s[3/2]_2^\circ$ metastable state. Background emission from the plasma-generated metastables (as opposed to Write-laser generated) represents a problematic optical interference at the same wavelength as the Read detection (830 nm) and necessitates a fine control over the Read laser energy and beam size/shape. Figure 6 shows raw data from measurements in the cathode plasma region as a function of laser time delay after subtracting the baseline (~2000 on this scale) along with their associated fits.

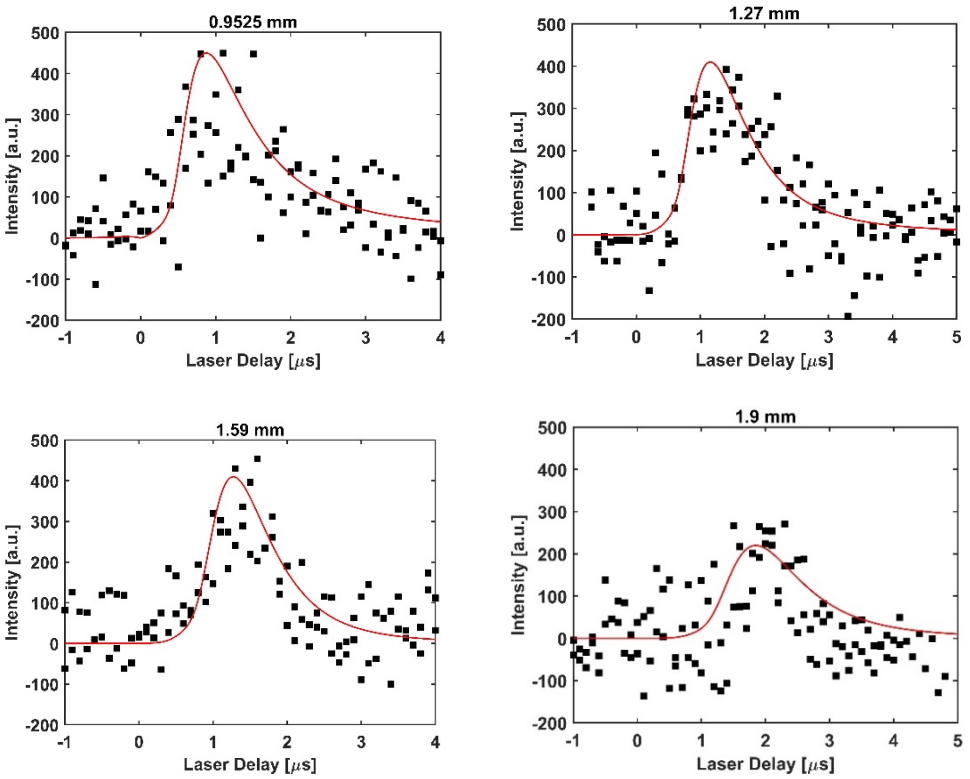

Fig. 6. Raw data (after baseline subtraction) for KTV within a plasma environment along with their associated fits. The different panels are for different spatial displacements as given in the panel title.

Following baseline subtraction, the signal to noise ratio (SNR) is ~5-6 where the SNR is defined by the peak value divided by the standard deviation in the baseline. (Baseline in this context refers to the baseline of the TALIF versus delay plots, not the raw PMT baseline.) The main factor causing the baseline variation is thought to be fluctuation of the probe laser and to a lesser extent time fluctuation in the metastable state population. However, even this SNR is on par or greater than what is commonly seen in other KTV applications where interference and/or

OPTICS CONTINUUM

signal quenching are present [41]. Figure 7 shows the best fit temperature and bulk velocity values associated with the fits in Fig. 6.

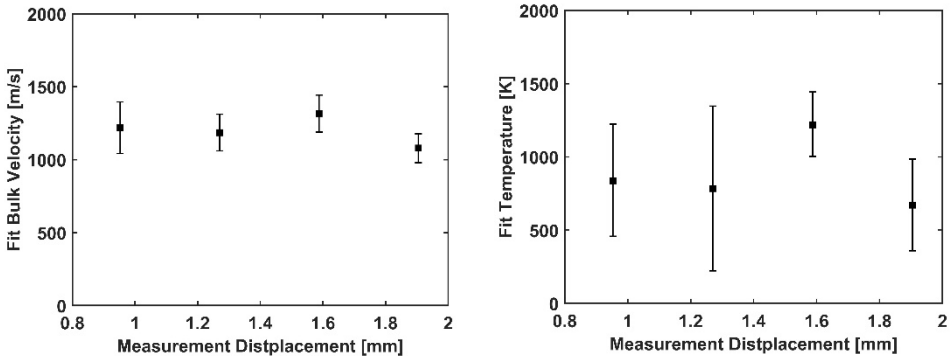

Fig. 7. Results of KTV within the plume of a plasma hollow cathode operating on krypton.

As discussed above, spatial variations are frozen such that we again report average properties, in this case velocity of 1200 ± 130 m/s and temperature of 880 ± 370 K. To the best knowledge of the authors, there is currently no published data regarding experimental measurements of the drift velocity or gas temperature for a plasma hollow cathode operating on krypton. However, there are several publications with both experimental and simulated data for hollow cathodes operating on argon and xenon which show a general agreement with the magnitude of both the velocity and the temperature. For example, Engeln et al. found the velocity and thermal temperature of ground state argon atoms from a cascaded arc plasma jet to be on the order of 2000 m/s and 1000 K [47]. Accounting for the different mass of krypton, these values align well with our results.

6. Conclusion

Accurate measurements of neutral atom properties, especially velocity distribution functions (VDFs), are required to validate development of numerical models within the electric propulsion community. The approach presented here can be a powerful compliment to existing VDF measurements based on (single-photon) LIF due to Doppler shifting of metastables. The KTV method can be advantageous in that the ground state velocity is directly probed (through direct movement of tagged atoms), thereby avoiding biases and resolution limits which can affect the Doppler method in certain cases. Results presented herein have been for the flow field of a hollow cathode, but similar measurements should be possible for Hall-effect thrusters, gridded ion thrusters, and other plasma devices of interest. We have shown application of KTV at chamber pressures down to $\sim 10^{-5}$ Torr representing a significant reduction (2-3 order of magnitude in comparison to previous KTV publications) in the required krypton number density needed for the method.

Future work will include an improved optical layout to achieve lower measurement error and improve the signal-to-noise, particularly for measurements within plasmas where competing luminosity is present. The main modification will be to switch to a narrow linewidth tunable diode laser for the Read step [35,37,41] instead of the OPO now used. The OPO laser provides Read illumination that is unnecessarily spectrally bright, given that it is orders of magnitude above saturation, meaning that it is difficult to avoid LIF excitation of the surrounding background plasma region (versus preferential light collection only in regions where tagged metastables are present). The more stable spatial profile of such a diode laser will also benefit S:N by allowing better control of the beam focusing.

OPTICS CONTINUUM

Future work will also expand the gas tagging velocimetry to the widely used xenon propellant. The proposed tagging scheme for xenon will use a Write step of two-photon excitation at 252.5 nm ($5P^6\ ^1S_0 \rightarrow 6p\ [3/2]_{2)}$) which decays into the $6s[3/2]^\circ_2$ metastable state with a branching ratio of 0.7, producing a florescence at 823.2 nm [50]. The 252.5 nm TALIF excitation of xenon has a similar two-photon absorption cross-section and branching ratio for the metastable populating transition as the 214.7 nm TALIF excitation of krypton studied in this work [41,50–52]. The xenon scheme should populate the metastable state at similar rates as seen within the current krypton work. The Read step will consist of a single photon excitation at 823.2 nm ($6s[3/2]^\circ_2 \rightarrow 6p\ [3/2]_{2)}$) with detection florescence recorded at either 823.2 nm (as is commonly used in LIF Doppler velocimetry [23]) or at 895.2 nm ($6p\ [3/2]_2 \rightarrow 6s[3/2]^\circ_1$), with the latter providing non-resonant detection albeit with weaker signal strength.

Funding. National Aeronautics and Space Administration (80NSSC21K1118).

Acknowledgments. The authors acknowledge the help of Seth Thompson and Dr John Williams, from Colorado State University, for supplying the plasma hollow cathode used in this work as well as their expertise in the setup and operation of the hollow cathode test facility. The authors also acknowledge funding support from NASA through the Joint Advanced Propulsion Institute, a NASA Space Technology Research Institute, grant number 80NSSC21K1118.

Disclosures. The authors declare no conflicts of interest.

Data availability. The data that support the findings of this study are available from the corresponding author upon reasonable request.

References

1. D. M. Goebel and I. Katz, *Fundamentals of Electric Propulsion: Ion and Hall Thrusters* (Wiley, 2008).
2. H. Baránková and L. Bardos, "Hollow cathode and hybrid plasma processing," Vacuum **80**(7), 688–692 (2006).
3. A. Lunk, "Plasma activated physical vapour deposition (PAPVD) by hollow cathode arc (HCA)," Vacuum **41**(7-9), 1965–1967 (1990).
4. Y. S. Kuo, R. F. Bunshah, and D. Okrent, "Hot hollow cathode and its applications in vacuum coating: a concise review," Journal of Vacuum Science & Technology A: Vacuum, Surfaces, and Films **4**(3), 397–402 (1986).
5. P. P. Deichuli, G. F. Abdrashitov, A. A. Ivanov, *et al.*, "Ion source with LaB6 hollow cathode for a diagnostic neutral beam injector," Rev. Sci. Instrum. **77**(3), 03B514 (2006).
6. C. C. Tsai, G. C. Barber, C. W. Blue, *et al.*, "Development of a long-pulse (30-s), high-energy (120-keV) Ion source for neutral beam applications," Nuclear Technology - Fusion **4**(2P3), 1424–1429 (1983).
7. D. M. Goebel and A. T. Forrester, "Plasma studies on a hollow cathode, magnetic multipole ion source for neutral beam injection," Rev. Sci. Instrum. **53**(6), 810–815 (1982).
8. S. Cong, R. Wu, L. Mu, *et al.*, "A 2D model for low-pressure hollow cathode arc discharges in argon," J. Phys. D: Appl. Phys. **52**(4), 045205 (2019).
9. I. Mikellides, I. Katz, K. Jameson, *et al.*, "Numerical simulations of a Hall thruster hollow cathode plasma," in *International Electric Propulsion Conference, IEPC* (2007).
10. I. G. Mikellides, A. Lopez Ortega, D. M. Goebel, *et al.*, "Dynamics of a hollow cathode discharge in the frequency range of 1–500 kHz," Plasma Sources Sci. Technol. **29**(3), 035003 (2020).
11. D. M. Goebel, G. Becatti, I. G. Mikellides, *et al.*, "Plasma hollow cathodes," J. Appl. Phys. **130**(5), 050902 (2021).
12. G. Sary, "Hollow cathode modeling: II. physical analysis and parametric study," Plasma Sources Sci. Technol. **26**(5), 055008 (2017).
13. I. Katz and I. G. Mikellides, "Neutral gas free molecular flow algorithm including ionization and walls for use in plasma simulations," J. Comput. Phys. **230**(4), 1454–1464 (2011).
14. W. A. Hargus and M. A. Cappelli, "Laser-induced fluorescence measurements of velocity within a Hall discharge," Appl. Phys. B: Lasers Opt. **72**(8), 961–969 (2001).
15. E. Beiting, R. Spektor, and K. Diamant, "Near field maps of xenon ion velocity of the SPT-140 Hall thruster by laser induced fluorescence," 33rd *International Electric Propulsion Conference, IEPC-2013-053* (2013).
16. R. J. Cedolin, W. A. Hargus, P. V. Storm, *et al.*, "Laser-induced fluorescence study of a xenon Hall thruster," Appl. Phys. B: Lasers Opt. **65**(4-5), 459–469 (1997).
17. C. Eichhorn, L. Pietzonka, F. Scholze, *et al.*, "Single- and two-photon absorption laser-induced fluorescence spectroscopy in rare gases for gridded ion thruster diagnostics," EPJ Techn Instrum **9**(1), 2 (2022).
18. L. Pietzonka, C. Eichhorn, F. Scholze, *et al.*, "Laser-induced fluorescence spectroscopy for kinetic temperature measurement of xenon neutrals and ions in the discharge chamber of a radiofrequency ion source," J Electr Propuls **2**(1), 4 (2023).
19. J. Walker, S. Langendorf, M. Walker, *et al.*, "Velocimetry of cathode particles in a magnetoplasmadynamic thruster discharge plasma," Rev. Sci. Instrum. **86**(7), 073513 (2015).
20. C. Farnell, D. L. Brown, G. Willis, *et al.*, "Remote diagnostic measurements of Hall thruster plumes," in *IEPC-2009-031* (2009).

OPTICS CONTINUUM

21. S. J. Thompson, S. C. Farnell, C. C. Farnell, *et al.*, "Combined electrostatic analyzer—Wien filter probe for characterization of species distributions in Hall thrusters," J. Appl. Phys. **130**(23), 233302 (2021).
22. V. H. Chaplin, R. B. Lobbia, A. Lopez Ortega, *et al.*, "Time-resolved ion velocity measurements in a high-power Hall thruster using laser-induced fluorescence with transfer function averaging," Appl. Phys. Lett. **116**(23), 234107 (2020).
23. M. F. Konopliv, V. H. Chaplin, L. K. Johnson, *et al.*, "Accuracy of using metastable state measurements in laser-induced fluorescence diagnostics of xenon ion velocity in Hall thrusters," Plasma Sources Sci. Technol. **32**(1), 015009 (2023).
24. I. Romadanov, Y. Raitses, A. Diallo, *et al.*, "On limitations of laser-induced fluorescence diagnostics for xenon ion velocity distribution function measurements in Hall thrusters," Phys. Plasmas **25**(3), 033501 (2018).
25. B. A. Jorns, M. Byrne, P. Roberts, *et al.*, "Prediction and mitigation of the mode transition in a magnetically shielded Hall thruster at high-specific impulse and low power," in *IEPC-2022-372* (2022).
26. J. Gottfried, S. Antozzi, C. Dumitrache, *et al.*, "Preliminary krypton measurements by two-photon absorption laser induced fluorescence (TALIF) in cold flow and a hollow cathode plasma," in *AIAA SCITECH 2023 Forum* (American Institute of Aeronautics and Astronautics, 2023).
27. T. Wegner, S. J. Thompson, J. Williams, *et al.*, "Two-photon absorption laser induced fluorescence (TALIF) of neutral xenon in a Hall effect thruster plasma," in *AIAA Propulsion and Energy 2021 Forum* (American Institute of Aeronautics and Astronautics, 2021).
28. C. Eichhorn, F. Scholze, D. Spemann, *et al.*, "Two-photon laser-induced fluorescence measurements of neutral densities near the accelerator grid of an ion thruster: status of current activities," in *International Electric Propulsion Conference, IEPC* (2022).
29. M. E. Galante, R. M. Magee, and E. E. Scime, "Two photon absorption laser induced fluorescence measurements of neutral density in a helicon plasma," Phys. Plasmas **21**(5), 055704 (2014).
30. S. Antozzi, J. A. Gottfried, J. D. Williams, *et al.*, "Spatially resolved measurements of krypton by two-photon absorption laser induced fluorescence (TALIF) in a barium oxide hollow cathode plasma," in *AIAA Aviation 2023 Forum* (American Institute of Aeronautics and Astronautics, 2023).
31. R. B. Miles, J. Grinstead, R. H. Kohl, *et al.*, "The RELIEF flow tagging technique and its application in engine testing facilities and for helium-air mixing studies," Meas. Sci. Technol. **11**(9), 1272–1281 (2000).
32. D. N. Hill, *Wave-modified Ion Distributions And Cross-field Transport Measurements By Laser-induced Fluorescence (optical-tagging, Ion-cyclotron Waves)*, (University of California, Irvine, 1983).
33. R. A. Stern, D. N. Hill, and N. Rynn, "Direct ion-transport measurement by optical tagging," Phys. Lett. A **93**(3), 127–130 (1983).
34. N. J. Parziale, M. S. Smith, and E. C. Marineau, "Krypton tagging velocimetry of an underexpanded jet," Appl. Opt. **54**(16), 5094 (2015).
35. M. A. Mustafa and N. J. Parziale, "Simplified read schemes for krypton tagging velocimetry in N_2 and air," Opt. Lett. **43**(12), 2909 (2018).
36. D. Zahradka, N. J. Parziale, M. S. Smith, *et al.*, "Krypton tagging velocimetry in a turbulent Mach 2.7 boundary layer," Exp. Fluids **57**(5), 62 (2016).
37. D. Shekhtman, W. M. Yu, M. A. Mustafa, *et al.*, "Freestream velocity-profile measurement in a large-scale, high-enthalpy reflected-shock tunnel," Exp. Fluids **62**(5), 118 (2021).
38. N. Jiang, S. W. Grib, P. S. Hsu, *et al.*, "High-repetition-rate krypton tagging velocimetry in Mach-6 hypersonic flows," Appl. Opt. **61**(9), 2192 (2022).
39. S. W. Grib, N. Jiang, P. S. Hsu, *et al.*, "100 kHz krypton-based flow tagging velocimetry in a high-speed flow," Appl. Opt. **60**(6), 1615 (2021).
40. M. A. Dakka, G. Tsiminis, R. D. Glover, *et al.*, "Laser-based metastable krypton generation," Phys. Rev. Lett. **121**(9), 093201 (2018).
41. D. Shekhtman, N. J. Parziale, and M. A. Mustafa, "Excitation line optimization for krypton tagging velocimetry and planar laser-induced fluorescence in 200-220 nm range," in *AIAA Scitech 2021 Forum* (American Institute of Aeronautics and Astronautics, 2021).
42. M. A. Mustafa, D. Shekhtman, and N. J. Parziale, "Single-laser krypton tagging velocimetry (KTV) investigation of air and N_2 boundary-layer flows over a hollow cylinder in the Stevens shock tube," *AIAA Scitech 2019 Forum* (2019).
43. D. Shekhtman, M. A. Mustafa, and N. J. Parzial, "Single-laser krypton tagging velocimetry (KTV) investigation of air and N_2 boundary-layer flows over a hollow cylinder in the Stevens shock tube," in *Proceedings of the 32nd International Symposium on Shock Waves (ISSW32 2019)* (Research Publishing Services, 2019), pp. 967–991.
44. B. D. Prince, R. J. Bemish, and Y.-H. Chiu, "Emission-excitation cross sections relevant to krypton-propelled electric thrusters," J. Propul. Power **31**(2), 725–736 (2015).
45. A. Kramida and Y. Ralchenko, "NIST Atomic Spectra Database, NIST Standard Reference Database 78," (1999).
46. P.-Y. C. R. Taunay, C. J. Wordingham, and E. Y. Choueiri, "Total pressure in thermionic orificed hollow cathodes: controlling mechanisms and their relative importance," J. Appl. Phys. **131**(1), 013303 (2022).
47. R. Engeln, S. Mazouffre, P. Vankan, *et al.*, "Flow dynamics and invasion by background gas of a supersonically expanding thermal plasma," Plasma Sources Sci. Technol. **10**(4), 595–605 (2001).
48. E. Titov, D. Levin, N. Gimelshein, *et al.*, "Analysis of Different Approaches to Modeling Nozzle Flows in the Near Continuum Regime," in *46th AIAA Aerospace Sciences Meeting and Exhibit* (American Institute of Aeronautics and Astronautics, 2008).

OPTICS CONTINUUM

49. K. Gazeli, X. Aubert, S. Prasanna, *et al.*, "Picosecond two-photon absorption laser-induced fluorescence (ps-TALIF) in krypton: the role of photoionization on the density depletion of the fluorescing state Kr 5p′[3/2]2," Phys. Plasmas **28**(4), 043301 (2021).
50. H. Horiguchi, R. S. F. Chang, and D. W. Setser, "Radiative lifetimes and two-body collisional deactivation rate constants in Ar for Xe(5 *p* 56 *p*),Xe(5 *p* 56 *p*), and Xe(5 *p* 57 *p*) states," J. Chem. Phys. **75**(3), 1207–1218 (1981).
51. S. Kröll and W. K. Bischel, "Two-photon absorption and photoionization cross-section measurements in the 5 p 5 6p configuration of xenon," Phys. Rev. A **41**(3), 1340–1349 (1990).
52. K. Kinefuchi, Y. Nunome, S. Cho, *et al.*, "Two-photon absorption laser induced fluorescence with various laser intensities for density measurement of ground state neutral xenon," Acta Astronaut. **161**, 382–388 (2019).